Book Chapter

Anti-microbial Properties and Mechanisms of Mg(OH)$_2$ and Cu-Infused Mg(OH)$_2$ Nanoparticles on Polypropylene Surface

Saleh Alkarri*

School of Packaging, Michigan State University 448 Wilson Road, East Lansing, MI 48824-1223, USA

Corresponding Author: Saleh Alkarri, School of Packaging, Michigan State University 448 Wilson Road, East Lansing, MI 48824-1223, USA

This Book Chapter is a republication of an article published by Saleh Alkarri, et al. at International Journal of Clinical Virology in May 29, 2024. (Alkarri S, Frame M, Cairney J, Maddan L, Kim JH, et al. Investigating Anti-Bacterial and Anti-COVID-19 Virus Properties and Mode of Action of Pure Mg(OH)$_2$ and Copper-Infused Mg(OH)$_2$ Nanoparticles and Coated Polypropylene Surfaces. Int J Clin Virol. 2024; 8: 008-023).

How to cite this book chapter: Saleh Alkarri. Anti-microbial Properties and Mechanisms of Mg(OH)$_2$ and Cu-Infused Mg(OH)$_2$ Nanoparticles on Polypropylene Surface. In: Alexandru Vasile Rusu and Monica Trif, editors. Prime Archives in Polymer Technology: 2nd Edition. Hyderabad, India: Vide Leaf. 2024.

Conflict of Interest: None of the author have a conflict of interest.

Abstract

Robust anti-microbial surfaces which are non-toxic to users have widespread application in medical, industrial and domestic arenas. Magnesium hydroxide has recently gained attention as an anti-microbial compound which is non-toxic, biocompatible and environmentally friendly. Here we demonstrate melt compound and thermally embossed methods for coating polypropylene with $Mg(OH)_2$ nanoplatelets and copper-infused $Mg(OH)_2$ nanoplatelets. Polypropylene articles coated with $Mg(OH)_2$ nanoplatelets and copper-infused $Mg(OH)_2$ nanoplatelets exhibits a log 8 kill of *E.coli* within 24 hours. In addition, $Mg(OH)_2$ NPs suspension, at 0.25 % reduced SARSCoV-2 virus titers in the solution by 2.5×10^3 PFU/mL or 29.4 %, while the Cu-infused $Mg(OH)_2$ NPs suspension, at 0.25 % reduced titers by 8.1×10^3 PFU/mL or 95.3 %. Fluorescence microscopy revealed that reactive oxygen species (ROS) are produced in bacteria in response to $Mg(OH)_2$ and Cu-infused $Mg(OH)_2$ nanoplatelets which appears to be an important but not the sole mode of anti-microbial action of the nanoplatelets. Plastics with anti-microbial surfaces from where biocides are non-leachable are highly desirable. This work provides a general fabrication strategy for developing anti-microbial plastic surfaces.

Keywords

Anti-Microbial Activity; *E. coli* K-12 MG1655; Anti-Viral Activity; SARS-CoV-2; Copper-Infused Magnesium Hydroxide; Non-Leachable; ROS; Compounding; Surface Embossing; Dyes

Introduction

Approximately 7.7 million people die from bacterial infections every year [1]. Infection due to antibiotic-resistant bacteria (ARB) is increasing, and 5 million deaths were associated with ARB in 2019 [2]. Therefore, limiting the spread of pathogenic bacteria is a matter of urgent concern. Viruses are causative agents of an estimated 60% of human infections across the globe [3]. Downregulation of the gut bacteria ecosystems has been linked to many prolonged diseases and conditions [4]. Infectious diseases may spread across an ecosystem, whether they originate from animals or humans, and spread mainly by ingestion but can even infect a person through skin contact in sporadic cases [5]. These viruses enter the surroundings through various channels, notably rainwater and chemicals [6,7]. Anti-microbial surfaces can limit the spread of disease as they can minimize microbial adhesion, destroy pathogens, and render hospitals simpler to disinfect [8]. This strategy is also considered to be distinct from the conventional techniques employed to reduce illness propagation, such as cleaning agents and antibiotics [9]. In addition, anti-microbial coatings can reduce our dependency on antibiotics [10]. Furthermore, since certain coatings can act through multiple mechanisms including physical disruption of pathogens, the bacteria are significantly less likely to evolve tolerance to them [11]. However, leaching of certain ions from surfaces can have toxicological implications and there is a concern for the capacity of anti-microbial resistance (AMR) to foster the rise of antibiotic resistant bacteria [7]. Surfaces coated with insoluble, non-leaching anti-microbials would offer a remedy to this emerging problem. Robust anti-microbial surfaces which are non-toxic to users have widespread application in medical, industrial and domestic arenas. Magnesium hydroxide has recently gained attention as an anti-microbial compound which is non-toxic, biocompatible and environmentally friendly.

There are three categories of anti-microbial agents which can be classified as either natural, organic, or inorganic. Natural anti-microbials, such as those found in rosemary, sage and basil, have a wide application and can be applied as surfactants to vegetables and fruits to ensure protection, safety, and quality and to extend

the shelf life [12]. While natural anti-microbial agents may present opportunities, they also carry along risks. Some natural anti-microbial substances may affect an individual's health and, in some cases, act as a poison since they are endocrine disruptors which are normally associated with developmental and reproductive harm [13]. Organic anti-microbials, such as lactic acid, play a vital role in the production of food for animals and the protection of public health, while the irresponsible use of these products may cause anti-microbial resistance [14]. This is one of the disadvantages of using organic anti-microbials [13]. Organic anti-microbials such as propionic acid and potassium sorbate are commonly used on farms. Inorganic anti-microbials, such as Longbei inorganic antibiotic powder, also play an essential role in our society. They can be used on farm and home equipment to prevent the spread of viruses and bacteria since they damage the physical features of the bacteria and viruses [15]. However, these agents typically contain some chemicals that might harm human health if they are toxic [13].

Inorganic anti-microbial materials have been classified as "leachable" and "non-leachable" [15]. Leachable anti-microbial agents, such as silver and copper are incorporated into plastics via melt-blending. Such leachable anti-microbial agents exhibit their anti-microbial properties by the release of the agents from polymers via leaching to the surrounding [16]. Unfortunately, leachable anti-microbial agents are often considered to be toxic to human cells and cannot be used at high concentrations, especially in food contact applications [17].

$Mg(OH)_2$ particles have recently attracted significant attention due to their widespread use as environmentally friendly anti-microbial agents [18]. $Mg(OH)_2$ is used in many areas, such as in suspensions as a laxative or antacid, and in wastewater treatment across the globe [19]. In this treatment, $Mg(OH)_2$ has a vital role in killing bacteria and viruses that might survive in the wastewater [18]. $Mg(OH)_2$ can be used as an antacid with other medications to relieve acid indigestion, heartburn, and upset stomach [20]. In some cases, $Mg(OH)_2$ is recommended for use during organ transplants. For example, $Mg(OH)_2$ and its carriers can be used in surgery to prevent catheter-associated urinary tract infection

(UTI) [21]. $Mg(OH)_2$ is also used as a laxative for adults and children to alleviate short-term constipation. $Mg(OH)_2$ belongs to the class of drugs known as saline laxatives, and it functions by inducing the stool to hold water [15]. Because their high fluorescence characteristic corresponds to their hydroxide composition, $Mg(OH)_2$ can also be employed in transplant systems such as biodegradable transplant gadgets for the human body and can consequently be utilized to monitor their disintegration and operational anti-bacterial potential. Additionally, their pH-responsive fluorescence shift can operate as a pH sensor for wound acidity, a hallmark of successful healing [22].

$Mg(OH)_2$ NPs are attractive materials for developing anti-microbial applications. However, few investigations have been conducted to study the anti-microbial mechanisms of $Mg(OH)_2$ NPs [23]. Cu-infused $Mg(OH)_2$ is a novel material (developed by Aqua Recourses Corp, Patent No: US20220225610A1), and its mechanism has not been studied previously. A plausible mechanism through which $Mg(OH)_2$ exhibits its anti-microbial activity might be immediate bacterial cell wall destruction or the availability of highly saturated OH groups on the exterior of $Mg(OH)_2$ NPs, which could harm the cell walls of bacteria. $Mg(OH)_2$ NPs may bind to the bacterial cell membrane through electrostatic interactions and then undermine the stability of the cell walls, resulting in the bacteria's death [24]. Bactericidal testing has revealed that anti-microbial efficacy depends upon the size of $Mg(OH)_2$ aggregates [25]. Transmitted electron microscopy (TEM) observations have not shown indications of cellular incorporation; instead, the anti-bacterial action is related to the degradation of cell wall stability [19]. The sticking ability of $Mg(OH)_2$ on the bacterial membrane might improve the permeability of cell walls, according to SEM and zeta prospective studies [26]. When all of these factors are considered, the anti-bacterial activity of nano-$Mg(OH)_2$ might be as follows: Nano-$Mg(OH)_2$ are initially deposited onto the bacterial membrane via charging affinity and then, by disrupting the stability of the cellular membranes, culminates in the bacteria's mortality [27].

Some metal NPs are capable of generating reactive oxygen species (ROS) in cells with which they interact. A detailed discussion of their chemistry has been reviewed recently by Čapek and Roušar [28]. The increased proliferation of infectious illnesses caused by microorganisms found in medical devices, food packaging, water treatment systems, and domestic appliances has elicited increased interest in the development of anti-microbial agents [5]. $Mg(OH)_2$ NPs kill rapid growing and highly persistent *Escherichia coli* (*E. coli*) cells by causing physical damage to the bacteria [29]. This effect is usually tested in aqueous bacteria liquid suspension where the $Mg(OH)_2$ particles come into contact with the bacteria in liquid suspensions [30]. When viewed under a microscope, it is evident that $Mg(OH)_2$ NPs cause physical damage to the bacteria [17]. The anti-microbial activity of $Mg(OH)_2$ NPs was investigated in vitro using *E. coli*, and was shown to significantly inhibit the growth of *E. coli* by promoting nucleic acid leakage, inhibiting protein synthesis, suppressing metabolic activity, and inducing the macrophages to generate ROS [31].

The non-leachable anti-microbial agents such as $Mg(OH)_2$ and Cu-infused $Mg(OH)_2$ have received less attention as candidates for polymer based applications because of their low anti-microbial properties. The poor performance of non-leachable anti-microbial agents corresponds to incorporation into plastics via melt-blending, which fully embeds these NPs in plastic matrix [32]. This embedding prevents the interaction between the biocidal particles and the bacteria because the polymer will act as a layer of insulation [33]. Although these anti-microbials can effectively kill the bacteria or virus by mediating the anti-microbial effect by chemical interaction, they require a direct physical contact with the microbe in order to directly attack the cell wall of the bacteria and fatally injure the cell [18].

In this study, melt blending as well as thermal surface embossing approaches were employed to incorporate $Mg(OH)_2$ and Cu-infused $Mg(OH)_2$ particles into PP and their anti-bacterial properties were investigated against *E. coli* K-12 MG1655 over periods of 0, 4, and 24 h. Similarly, anti-viral activity of pure $Mg(OH)_2$ and Cu-infused $Mg(OH)_2$ NPs were studied against SARS-CoV-2 for 4 h to evaluate their properties. The biocidal

mechanisms of these anti-microbial agents were studied against *E. coli* K-12 MG1655 by measuring the total cellular ROS in the bacteria. In addition, the anti-viral properties were assessed against SARS-CoV-2. The PP samples were furtherly characterized by differential scanning calorimetry (DSC), thermogravimetric analysis (TGA), scanning electron microscopy (SEM), and energy dispersive X-ray spectroscopy (EDX).

Experimental
Materials

Polypropylene homopolymer (PP 500 P grade) was supplied by SABIC (Riyadh, Saudi Arabia) as powder (used for melt-compounding) and pellets (used for film extrusion) having the following characteristics: melting point = 166 °C, density = 905 kg/m^3, and melt flow index (MFI) measured at 230 °C and 2.16 kg = 3 g/min. $Mg(OH)_2$ (purity: 99.99 %) and Cu-infused $Mg(OH)_2$ (purity: 99.99 %) were supplied by Aqua Resources Corp (Florida, USA) as a dry powder of $Mg(OH)_2$ (used for melt-compounding) and slurry of (i) $Mg(OH)_2$ and (ii) Cu-infused $Mg(OH)_2$ (suspended in water used for thermal surface embossing). Isopropyl alcohol was obtained from Macron Fine Chemicals (purity: 99.99 %). Dulbecco's Modified Eagle Mediam (DMEM), Avicel, phosfate-buffered saline (PBS), and L-glutamine were obtained from commercial suppliers. The total cellular reactive oxygen species (ROS) concentration in the bacteria was detected using the Image-iT^{TM} LIVE Green Reactive Oxygen Species Detection Kit (ThermoFisher Scientific, catalog number I36007), which included 5-(and-6-)-carboxy-2',7'-dichlorodihydrofluorescein diacetate (carboxy-H_2DCFDA) for ROS detection, the cell-permeant nucleic acid stain Hoechst 33342 to identify individual bacteria, and *tert*-butyl hydroperoxide (TBHP) which is a common inducer of ROS production and serves as positive control.

Methods

Melt-Compounding and Injection Molding of PP with the Anti-Microbial NPs

The anti-microbial NPs were mixed manually with the PP powder and extrusion compounded using a DSM Xplore 15cc Micro extruder that was equipped with co-rotating conical twin screws (processing temperature: 250 °C, speed: 10 rpm, time: 2 min). The mixing ratio was PP with 5 wt.% of $Mg(OH)_2$ and PP with 5 wt.% of Cu-infused $Mg(OH)_2$. Extrusion compounding led to PP composites containing the biocidal additives at the desired level. The neat PP (without biocide) and PP composites were injected into disk-shape samples (dimensions: 25 mm diameter and 1.55 mm in thickness) using a 3.5 mL. Injection molder (**Figure 1**). The temperature of the cylinder was set at 250 °C and the mold temperature was fixed at 60 °C.
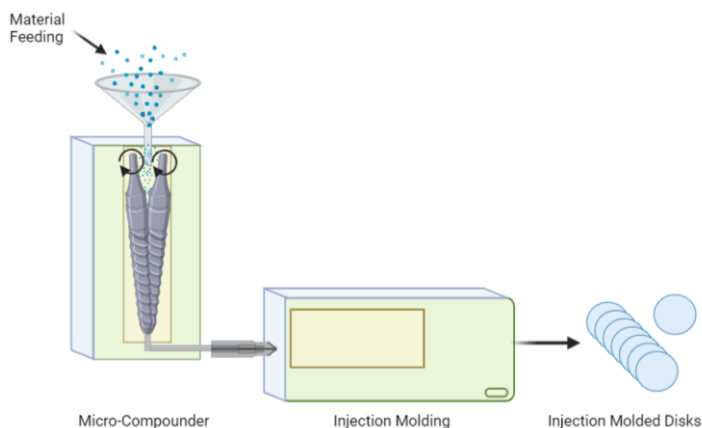
Figure 1: Micro-compounder and injection molding unit.

Coating of NPs on PP Surface
A) Coating Solution Preparation:

The $Mg(OH)_2$ NPs were obtained commercially as a slurry (7 wt.% $Mg(OH)_2$ and 93 wt.% water). The $Mg(OH)_2$ slurry (14.3 mL) was diluted with isopropyl alcohol (85.7 mL) to prepare a $Mg(OH)_2$ suspension at a concentration of 10 mg/mL (**Figure 2**). The suspension was vortexed at its maximum speed for 30s, and

subsequently sonicated in an ultrasonic bath at 23 °C for 10 min to ensure that the $Mg(OH)_2$ NPs were uniformly dispersed. After sonication, the suspension was vortexed once more at the maximum speed for 30 s.

The Cu-infused $Mg(OH)_2$ NPs were obtained commercially as a slurry (7.47 wt.% Cu-infused $Mg(OH)_2$ and 92.53 wt.% water). The Cu-infused $Mg(OH)_2$ slurry (1.34 mL) was diluted with isopropyl alcohol (8.66 mL) to prepare a Cu-infused $Mg(OH)_2$ suspension at a concentration of 10 mg/mL (**Figure 2**). The suspension was vortexed at a maximum speed for 30 s, and subsequently sonicated in an ultrasonic bath (Branson 2510 Ultrasonic Sonicator, Commack, NY, USA) at 23 °C for 10 min to ensure that the Cu-infused $Mg(OH)_2$ NPs were uniformly dispersed. After sonication, the suspension was vortexed once more at the maximum speed for 30 s.
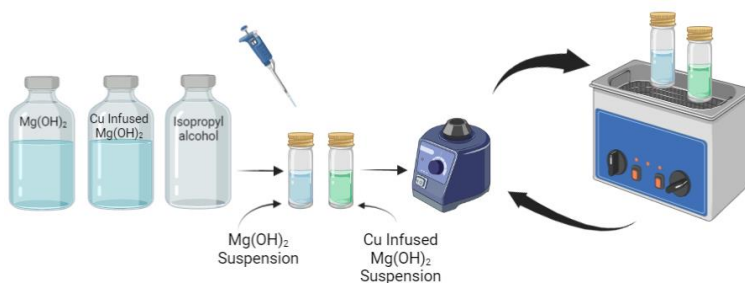
Figure 2: Preparation of the anti-microbial suspension.

## B) Deposition of the NPs onto Aluminum Foil:

A metallic rod applicator technique (K303, RK Print Coat Instruments Ltd., UK) was used to deposit the anti-microbial biocidal suspension over the aluminum foil (All-Foils, Inc. OH, USA, Dimension: 0.00762x30.48x 30.48 cm) (**Figure 3**). The thickness of the wet deposited coating varied between 4-120 microns depending on the diameter of the wire. The anti-microbial suspension was spread as a wet film deposition over an aluminum foil (via 5 mL syringe) using the metallic rod number 5, corresponding to a thickness of 50 microns, and left to dry at 23 °C for 10 min.
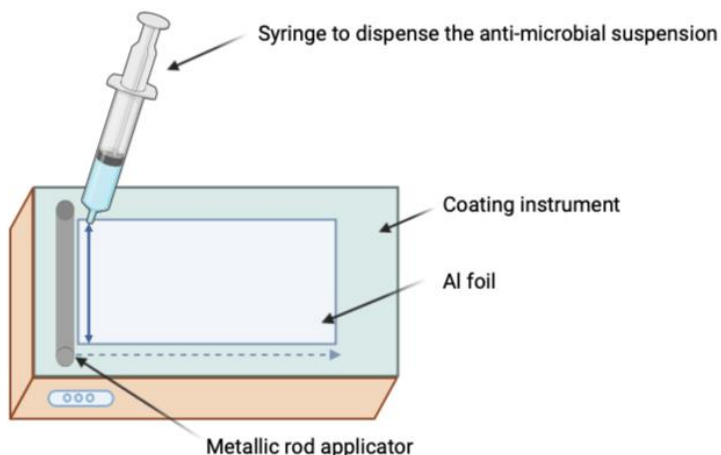
Figure 3: Deposition of the anti-microbial suspension onto a substrate using a metallic rod applicator.

C) Thermal embossing of NPs on PP Surfaces:

Disks were cut (Dimension: 20 mm in diameter, 0.5 mm in thickness) from PP extruded sheets (neat PP without biocides) using a Kongsberg X24 Edge Cutting Table, and from metallic copper sheets (Szone brand, China) using a Brother HS-70 A (wire EDMs) cutter device. Coated aluminum foil with anti-microbial crystals was used to transfer the temporarily deposited particles to the surface of the PP disks prior to the thermal embossing process where the particles were permanently fixed over the PP disk surfaces. The coated side of the aluminum foil was placed in contact with the PP (**Figure 4**) and pressed above the softening temperature of the PP using a compression molding press (PHI QL438-C, City of Industry, CA, USA). A temperature of 143 °C and 2 bars of pressure for 10 s were used for the PP disks.
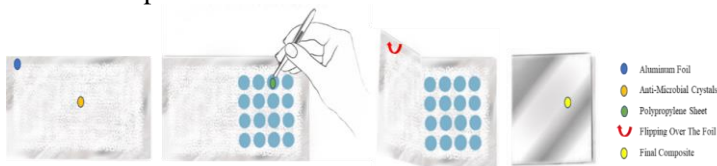
Figure 4: Transfer of anti-microbial particles to the surface of PP disks using coated aluminum foil prior to compression molding.

Characterization

Scanning Electron Microscopy (SEM) and Energy Dispersive X-Ray (EDX) Preparation Methods

The anti-microbial particles (powders of $Mg(OH)_2$ and Cu-infused $Mg(OH)_2$), the compounded and injection molded PP disks (5 % $Mg(OH)_2$ and 5 % Cu-infused $Mg(OH)_2$ by weight), and the thermally embossed disks (suspesion of $Mg(OH)_2$, and Cu-infused $Mg(OH)_2$ at 10 mg/mL) were characterized by SEM using a JEOL 7500F field emission emitter (JEOL Ltd., Tokyo, Japan), and by EDX analysis using an Oxford Instruments Aztec system (Oxford Instruments, High Wycomb, Bucks, England). Samples for EDX analysis were prepared by mounting samples on aluminum stubs affixed with epoxy glue. All mounted samples were coated with iridium (at a thickness of ~ 2.7 nm) by means of a Quorum Technologies/Electron Microscopy Sciences Q150T turbo pumped sputter coater (Quorum Technologies, Laughton, East Sussex, England BN8 6BN) and purged with argon gas.

Differential Scanning Calorimetry (DSC)

The melting point and the crystallization temperature of the PP samples were determined by DSC using a TA Instrument Model Q100 system. The nitrogen flow was set at 70 mL min^{-1} for all measurements. The samples were thermally analayzed in the temperature range of -20 to 250 °C at a rate of 10 °C min^{-1} and held for 1 min to eliminate previous crystallization, mechanical, thermal, processing, and shear history. The samples were additionally cooled to -20 °C at a rate of 10 °C min^{-1} and then re-heated to 250 °C at 10 °C min^{-1} and the thermal responses were recorded. All samples were analysed in triplicate.

The degrees of crystallinity of the PP samples were calculated from the heat of fusion values determined from the **second heating** runs and evaluated according to Equation (1):

$$X_c(\%) = \left[\frac{\Delta H_c}{\Delta H_0 . W}\right] x 100 \qquad (1)$$

Where X_c is the crystallinity of the PP samples, ΔH_c is the heat of fusion, ΔH_0 is the enthalpy of fusion for 100 % crystalline PP [209 J/g] [34], and W is the fraction (weight) of PP in the composite.

Thermogravimetric Analysis (TGA)

Thermal characterization of the PP samples was conducting with a TA Instruments (Model Q 50) system via thermogravimetric analysis (TGA) techniques. A quantity of (7 ± 2 mg) of each sample was placed in an aluminum pan. The temperature was then ramped gradually from 25 to 600 °C at a heating rate of 10 °C min^{-1} under a nitrogen atmosphere with a flow rate of 40 mL min^{-1}. All samples were analysed in triplicate.

Anti-Microbial Testing Method

E. coli K-12 MG1655 was used for all experiments to evaluate the anti-microbial activities of the disks. Stock culture was stored at -80 °C in a ThermoFisher TSX400 system and applied as streaks onto Tryptic Soy Agar (TSA) plates (BBL/Difco, Sparks, MD, USA). After incubation at 37 °C for 24 h, a single colony was selected and transferred to 5 mL of Tryptic Soy Broth (TSB) (BBL/Difco, Sparks, MD, USA) and incubated at 37 °C for 18 h. After incubation, 1 mL of culture was centrifuged at 13,000 x *g* for 5 min using a Fisher Scientific accuSpin micro 17 R centrifuge and the supernatant was discarded. Cells were suspended in 1 mL of phosphate-buffered saline (PBS, Crystalgen, Innovation for Science, Commack, NY, USA) by vortexing. The cell suspension was then transferred to a 15 mL tube and 11.5 mL of PBS was added. Aliquots of this suspension were then exposed to the different types of disks. Each single disk was placed separately in a pod; a contact lens cases manufactured by Bosch + Lomb. For each pod containing a single disk, 1 mL of bacterial suspension was added to submerge the disk into the culture broth and the pods were closed. The pods were then attached to a mini rotator (Benchmark Scientific, Roto Mini Plus R 2024, Sayreville, NJ, USA) and rotated at 20 rpm (**Figure 5**) around the machine's horizontal axis to continuously agitate the broth and cause liquid renewal on the surface of the disks. At 0, 4, and 24 h intervals, a 100 mL sample of the bacterial suspension was removed for the

appropriate number of 1:10 dilutions, plated in TSA, and then incubated at 37 °C overnight. The colony forming units (CFU) were enumerated to determine the bacterial cell density at each timepoint (Scan300, InterScience). Neat PP disks were used as a "negative" control sample, while metallic copper disks were used as a "positive" control sample. In addition, the anti-microbial activity of different PP composite disks was tested individually.

Figure 5: The pods were attached with tape to the mini rotator device for consistent agitation of the bacterial broth and surface renewal of the disks inside the pods. The blue tray holding the pods rotates around the horizontal axis.

Anti-Viral Testing Method

$Mg(OH)_2$ NPs were prepared as described by Madden *et al*. [35] Cu-infused $Mg(OH)_2$ NPs were prepared according to (Maddan 2022) [36]. The solid contents of the suspensions was determined by a Satrorius Moisture Analyzer (MA35-SV2). The solid content of the $Mg(OH)_2$ NPs suspension was adjusted by addition of deionized water. $Mg(OH)_2$ was prepared at 2,780 ppm (vol. 3.6 mL), Cu-infused $Mg(OH)_2$ NPs were prepared at 2,780 ppm (vol. 3.6 mL) as concentrations suitable for dilution in subsequent steps.

The USA-WA1/2020 strain of SARS-CoV-2 was received from BEI Resources [37] and cultured on Vero E6 cells to establish master and working stocks. Virus stocks were determined to be free of mycoplasma and titers were determined by standard plaque assay on Vero E6 cells as described below. The identity of the

virus was confirmed by sequencing using the iSEQ 100 next generation sequencing platform (Illumina, SanDiego, USA).

All anti-viral experiments were conducted within the biosafety level 3 (BSL-3) in the Laboratory of Infectious Diseases, University of Southern Alabama. On the day of the experiment, SARS-CoV-2 virus was diluted in Dulbecco's phosphate-buffered saline (DPBS) to achieve 1 x 10^5 plaque forming units (PFU)/0.1 mL and kept on ice. Prior to use, the $Mg(OH)_2$ NPs suspension and Cu-infused $Mg(OH)_2$ NPs suspension were vortexed for 5 s prior to combining 0.9 mL of this suspension with 0.1 mL of virus in a 1.7 mL microcentrifuge tube to achieve final concentration of NPs 2,500 ppm. Cytotoxicity controls consisted of 0.9 mL of the test articles combined with 0.1 mL of DPBS alone. The virus control consisted of 0.1 mL of diluted virus in 0.9 mL of DPBS. Each treatment was performed in duplicate. Immediately following preparation, all samples were incubated at room temperature in a biological safety cabinet (BSC) with rotation to keep the NPs well dispersed. After 4 h, each sample tube was collected and stored at -80 ºC until needed for titration. Plaque Assay: Vero E6 cells were seeded in a 12-well plate until the cell confluency reached greater than 95 %. Samples were removed from a freezer that was operated at -80 ºC and allowed to thaw on ice before preparing 10-fold serial dilutions of each sample in virus diluent (DPBS containing 2% FBS). Duplicate wells of Vero E6 cells were then inoculated with 0.1 mL of each diluted sample and incubated at 37 °C with rocking every 15 min. After 1 h, cells were overlayed with DMEM containing 1.2 % Avicel, 2 % PBS and 1x L-glutamine and gently swirled. After 2 days of incubation at 37 °C with 5 % CO_2, cells were fixed by adding 0.5 mL of 10 % buffered formalin to each well and then incubating them for 1 h at room temperature. Formalin was decanted in a labeled hazardous waste container and enough 0.4 % crystal violet solution (~0.5 mL) was added to cover each well. After more than 1 minute of incubation at room temperature, plates were rinsed in a bucket filled with running tap water and tapped on absorbent material until the stain was visibly removed. Plates were inverted and allowed to air dry thoroughly before plaques were counted and used to calculate PFU/mL.

Confocal Microscopy to Study the Anti-Microbial Mechanism

E. coli K-12 MG1655 (American Type Culture Collection, Manassas, VA) was used for all experiments to evaluate and compare the anti-microbial mechanism of (i) biocidal particles, and (ii) PP disks that were thermally embossed with the biocidal particles. *E. coli* was first inoculated on the surface of TSA (solid medium) and incubated at 37 °C overnight. Monoclonal colonies were then picked and placed in the TSB (liquid medium) and shaken (MaxQ400, ThermoFisher) at 220 rpm overnight under aerobic conditions. The optical density of the bacterial solution was determined at OD 600 nm $[OD_{600}]$ = 0.92 to 105 colony-forming units/mL (CFU/mL).

Confocal fluorescence images were acquired using an Olympus FluoView 1000 Confocal Laser Scanning Microscope (Olympus Corporation, Tokyo, Japan) that was configured on an automated IX81 inverted microscope with a 60x Plan Apo N oil objective lens (NA 1.42). Image acquisition and analysis were performed using the Olympus FV10-ASW software (version 4.02.03.06). ROS-positive bacteria were detected by exciting the carboxy-H_2DCFDA using a 488 nm Argon laser line and recording the green fluorescence emission through a 505 nm long pass emission filter. Hoechst fluorescence was sequentially excited using a 405 nm diode laser and recorded through a blue 430-470 nm band pass filter. Transmitted light brightfield images of the bacteria were simultaneously recorded using the 488 nm laser line (data not shown). Metal NPs are capable of generating ROS in cells with which they interact. The chemistry of metallic NPs had been reviewed in detail by Čapek and Roušar [28].

A 250 mL aliquot of each bacterial sample was simultaneously labeled with 100 mM carboxy-H_2DCFDA (2.5 ml of 10mM carboxy-H_2DCFDA) and 20 mM Hoechst (5 mL of 1 mM Hoechst). Each sample was incubated for 30 min at 37 °C. The bacterial samples were then centrifuged to pellet the bacteria, and the supernatant was removed. The bacterial samples were then resuspended in 40 mL of deionized water and imaged by confocal microscopy. Positive ROS detection was indicated by green

fluorescence within the treated bacteria. For a positive ROS control, a 250 mL aliquot of a control bacterial sample was incubated with 400 mM TBHP (4 mL of 25 mM TBHP) for 90 min at 37 °C. The TBHP-treated samples were then simultaneously labeled with 100 mM carboxy-H_2DCFDA and 20 mM Hoechst for 30 min at 37 °C. The bacterial samples were then centrifuged to pellet the bacteria, and the supernatant was removed. The bacterial samples were then resuspended in 40 mL of deionized water and imaged by confocal microscopy (**Figure 6**). For each sample, an average of ten confocal fluorescence images were collected and analyzed in Image J software. Positive ROS-labeled cells (displayed in green color) were identified using the "multi-point" feature in Image J software. The total number of ROS-labeled cells were then counted for each image, and the average number of ROS positive cells for each set of samples was calculated and reported.
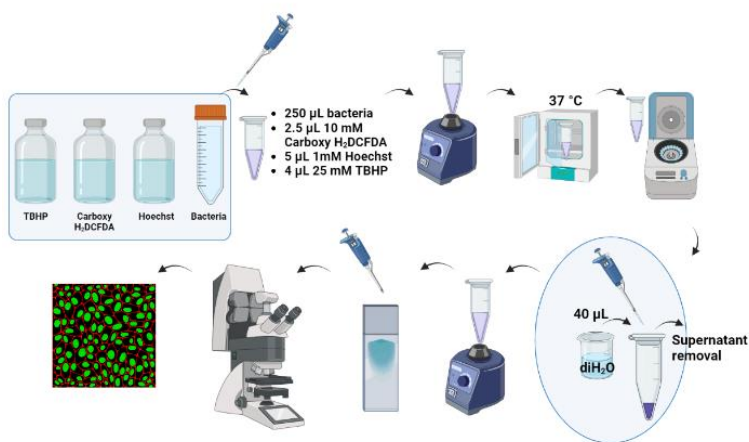
Figure 6: Carboxy-H_2DCFDA staining process.

Experimental Design and Statistical Analysis

A 2x2 factorial experiment was used to investigate the effect of the non-leachable anti-microbial agents ($Mg(OH)_2$, and Cu-infused $Mg(OH)_2$) based on the method of incorporation (compounding and thermal embossing) against *E. coli* K-12 MG1655.

All experiments were independently replicated using at least three biological replicates. Differences between the means of *E. coli* K-12 MG1655 cell density as affected by the direct exposure to the: (1) metallic copper disk (positive control), (2) neat PP disk (negative control), and (3) PP disks incorporating anti-microbial agents were compared at 0, 4, and 24 h using Tukey's honest significant difference test and Student's *t*-tests at a 96 % confidence level ($p \leq 0.05$). Interactions between the type of anti-microbial agent, methods of incorporating the anti-microbial agents with PP (compounding, thermal embossing), and anti-microbial activity were analyzed via four-way analysis of variance (ANOVA) using Origin 2022b software (ver. 9.9.5.167: OriginLab Corporation, Massachusetts, USA).

Results
Biocidal Crystals Characterization

The SEM images of the two selected inorganic biocides are presented in (**Figure 7** and **Figure 8**). The morphologies of the crystals in the compounded and injection molded disks and the thermal embossed disks are discussed and correlated with the disposition of the crystals in the PP.

## SEM and EDX Characterization of Pure Mg(OH)$_2$ NPs

The Mg(OH)$_2$ crystals are visually white in color. SEM analysis of the Mg(OH)$_2$ particles (**Figure 7**) shows the particles to be platelet-like in shape, and approximately 160-260 nm wide, with a thickness of 30-50 nm. The EDX specturum has confirmed the NPs type which is Mg.
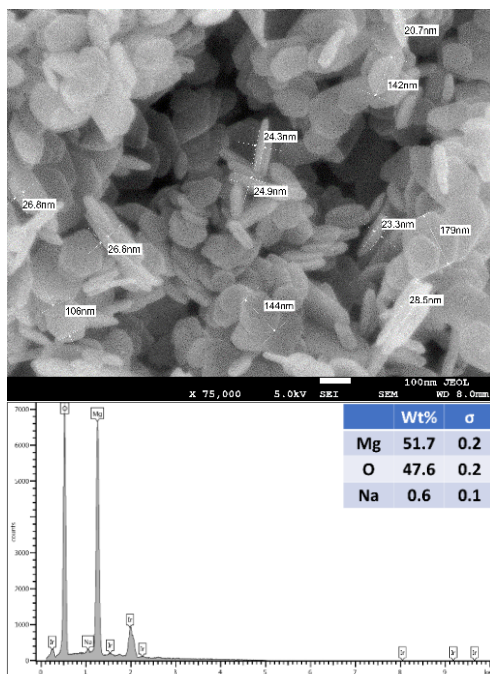
Figure 7: SEM image and EDX spectrum of the Mg(OH)$_2$ crystals.

SEM and EDX Characterization of Pure Cu-Infused Mg(OH)$_2$ NPs

The Cu-infused Mg(OH)$_2$ crystals are visually green in color. SEM analysis of the Cu-infused Mg(OH)$_2$ particles (**Figure 8**) shows some of the particles to be in a platelet form and others to have a spherical morphology, with each in close association. The platelet shaped particles represent the Mg(OH)$_2$ and had a width in the range of 160-260 nm and a thickness of 30-50 nm, while the spherical shaped particles represent the Cu and had diameters in the range of 100-280 nm. Both particles are mixed together and adhered to each other through their outer surfaces via electrostatic interactions.
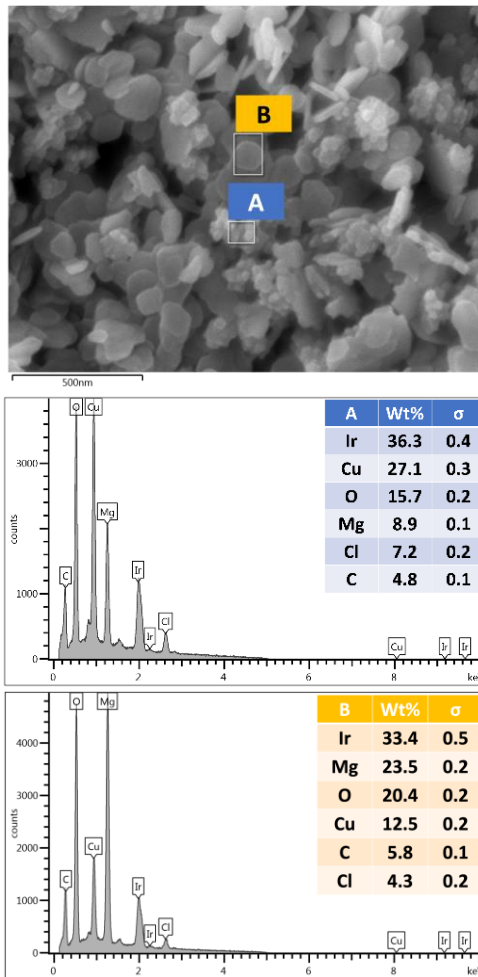
Figure 8: SEM image and EDX spectrum of the Cu-infused Mg(OH)$_2$ crystals.

The crystals have two different shapes; nanoplatelets for Mg(OH)$_2$, and spherical for Cu. Both crystals are attached together from the outer surface due to the ion exchange phenomena. The spectrum A was placed on the spherical crystals (**Figure 8**, **middle**, **inset**), and it revealed a higher weight percentage for Cu and a lower weight percentage for Mg. In contrast, when the spectrum B was placed on the platelet crystals (**Figure 8**, **right**, **inset**), it revealed a higher weight percentage for Mg and a lower weight percentage for Cu.

SEM and EDX Characterization of Melt-Compounded NPs
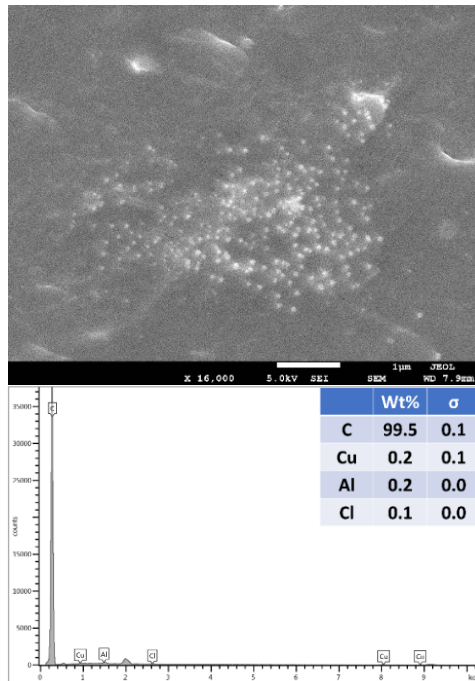
Side view (surface) of PP compounded with 5 wt.% Mg(OH)$_2$

The SEM image is presented in (**Figure 9**, **left**, **inset**) and EDX spectrum is in (**Figure 9**, **right**, **inset**).
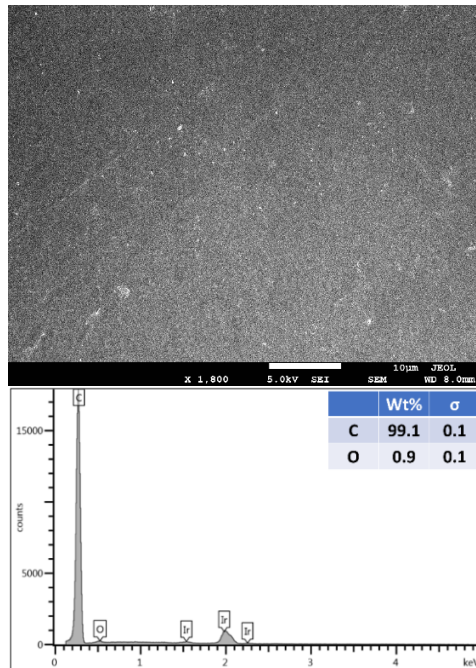
Figure 9: Side view (surface) of PP compounded with 5 wt.% Mg(OH)$_2$.

*Side view (surface) of PP compounded with 5 wt.% Cu-infused Mg(OH)$_2$*

The SEM image is presented in (**Figure 10**, **left**, **inset**) and EDX spectrum is in (**Figure 10**, **right**, **inset**).

	Wt%	σ
C	99.5	0.1
Cu	0.2	0.1
Al	0.2	0.0
Cl	0.1	0.0

Figure 10: Side view (surfase) of PP compounded with 5 wt.% Cu-infused $Mg(OH)_2$.

SEM and EDX Characterization of PP Disks with Thermally Embossed NPs

The SEM image provided in (**Figure 11**) shows the surface characteristics of an untreated PP disk (A), smooth packed surface of a PP disk that was thermally embossed with $Mg(OH)_2$ nanoplatelets (B), and the rougher surface of a PP disk that was thermally embossed with Cu-infused $Mg(OH)_2$ composed of nanoplatelets and spherical nanoparticles (C).
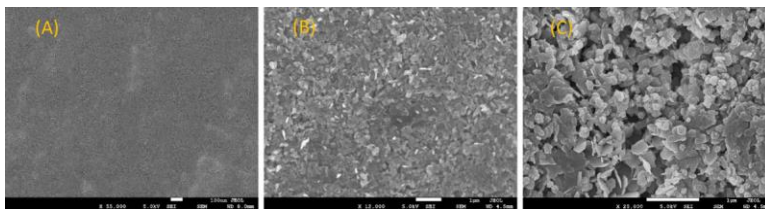
Figure 11: SEM images of (A) neat PP, (B) PP that was thermally embossed with $Mg(OH)_2$ NPs, and (C) PP that was thermally embossed with Cu-infused $Mg(OH)_2$ NPs.

Anti-Microbial Studies

Melt-Compounding and Injection Molding of PP with the Anti-Microbial Additives

PP disks (Dimensions: 25 mm diameter and 1.55 mm in thickness) constructed as described in **Section 2.2** were placed in pods containing approximately a log 8 *E. coli* in a volume of 1 mL PBS. The pods were rotated at 20 rpm at room temperature. 100 µL of the cultures were taken at 4 and 24 h and plated on TSA. Plates were incubated at 37 °C overnight and counted. Reduction in cell population within the pods were then calculated. The anti-microbial properties of NPs in PP melt-compounded articles are presented in (**Figure 12**).
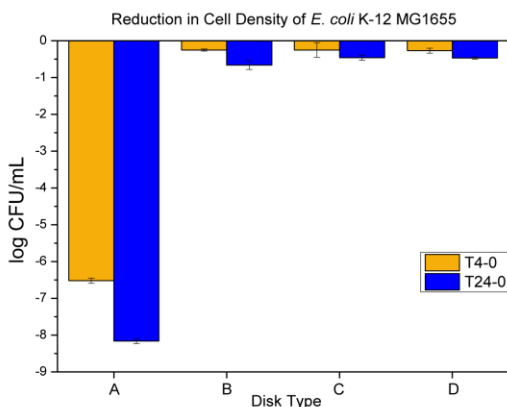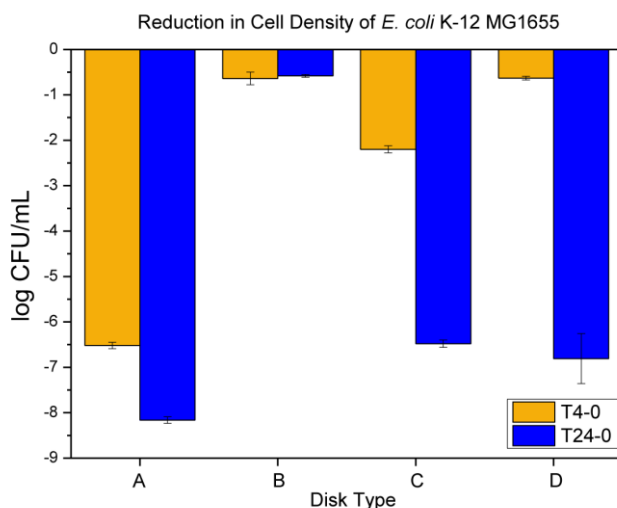

Figure 12: The anti-microbial data obtained for (A) metallic copper (positive control), (B) neat PP (negative control), (C) PP containing 5 wt.% $Mg(OH)_2$, and (D) PP containing 5 wt.% Cu-infused $Mg(OH)_2$.

No reduction in *E. coli* population was observed as a result of exposure to neither (i) $Mg(OH)_2$ nor (ii) Cu-infused $Mg(OH)_2$ (**Figure 12**). This finding demonstrates that there was no leaching of either agent from the interior of the compounded PP disks.

Thermally Surface Embossed NPs on the PP Surface and their Anti-Microbial Properties

After demonstrating that $Mg(OH)_2$ and Cu-infused $Mg(OH)_2$ NPs do not migrate from the interior of PP matrix to attack externally located bacterial cells, NPs were placed on the surfaces of PP disks and their anti-bacterial performance was evaluated. Disks embossed with $Mg(OH)_2$ NPs or Cu-infused $Mg(OH)_2$ NPs were placed in small pods to which a log 8 ± 0.16 of *E. coli* suspension in PBS was added. The pods were rotated at 20 rpm at room temperature and samples were taken, diluted, and plated at 4 and 24 h after commencement of the experiment. Colonies were counted after the plates had been incubated for 18 to 24 h and cell counts were plotted as shown in (**Figure 13**).


Figure 13: The anti-microbial data obtained for (A) metallic copper (positive control), (B) neat PP (negative control), (C) PP that had been thermally embossed with $Mg(OH)_2$ NPs, and (D) PP that had been thermally embossed with Cu-infused $Mg(OH)_2$ NPs.

When the NPs were on the surfaces of the PP disks, significant reductions in the bacterial population were observed, in which more than log 6 or over 99.99996 % kills are detected in a 24 h time frame as shown in (**Figure 13**). This finding indicates that these nanoplatelet materials are highly effective anti-microbial surface treatments. This work shows for the first time the use of Magnesium Hydroxide nanoplatelets as a robust and highly effective coating that my be applied to plastic surfaces post-manufacture. Given the safety of $Mg(OH)_2$ for human use, these results open up significant industrial possibilities.

Anti-Viral Characterization of Pure NPs

All experiments were conducted in BSL-3 containment. Cytotoxicity of the test specimens in the absence of virus was assessed by plating 0.1 mL of "test article only" samples and 10-fold dilutions on Vero E6 cells. As shown in (**Figure 14**), no evidence of cytotoxicity indicated by loss of staining with crystal violet was observed from DPBS as well as the $Mg(OH)_2$ NPs and Cu-infused $Mg(OH)_2$ NPs test specimens when they had been diluted from 10^{-1} to 10^{-3}. However, staining of cells in the very first well (undiluted) of these test specimens were lightened, indicating that cell lysis had occurred, and suggesting that 2500 ppm of $Mg(OH)_2$ NPs and Cu-infused $Mg(OH)_2$ NPs suspensions can cause cell damage (Note that cytotoxicity from $Mg(OH)_2$ NPs is marginal).
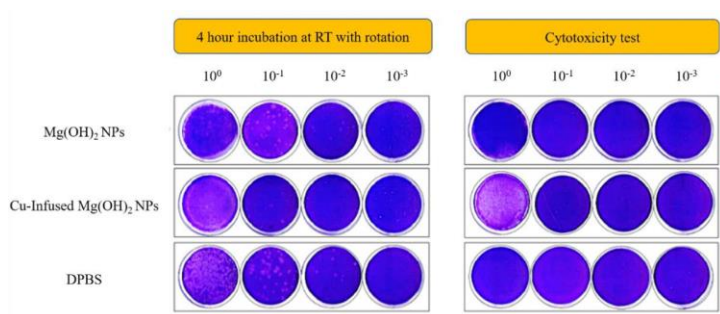
Figure 14: Plaque assays on Vero E6 cells: Infectivity of SARS-CoV-2 viruses incubated with NPs or DPBS. After the plaques had been assayed, cells were fixed with 10 % buffered formalin for 1 h, followed by crystal violet staining. After completing plaque-counting, plates were scanned. Images are representative of each condition.

Infectivity of SARS-CoV-2 viruses following incubation with test articles or DPBS (control) for 4 hours at room temperatures with rotation was measured by plaques assay on Vero E6 cells, as shown in (**Figure 14**). The numerical results from the plaque assays are presented in (**Figure 15**) infectivity of SARS-CoV-2 virus mixed with the control (DPBS) was maintained at 8.5×10^4 PFU/mL during the 4 h test period (**Figure 15**, **left**). In contrast viral titers in samples incubated with Cu-infused $Mg(OH)_2$ NPs were reduced to 4×10^2 PFU/mL during the same span of time. Titers were reduced to 6×10^4 PFU/mL when SARS-CoV-2 virus was incubated for 4 h in the presence of $Mg(OH)_2$ NPs. This represents a 95.3 and 29.4 % reduction, respectively, in SARS-CoV-2 virus infectivity under the tested conditions (**Figure 15**, **right**). These results show the Nanoplatelets are effective against both viruses and bacteria.
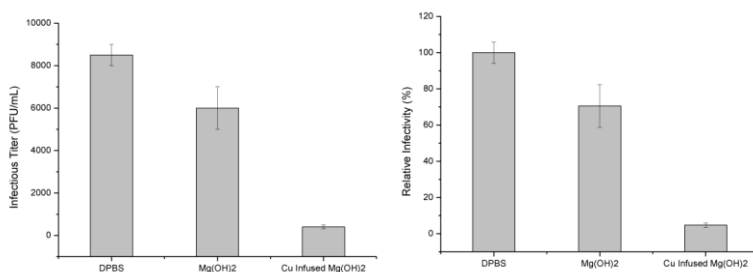
Figure 15: Inactivation of SARS-CoV-2 viral infectivity by incubation with the test specimens. The results shown on the left are plotted as viral titer (PFU/mL) and those shown at the right are plotted as percentage format (%). Relative value to DPBS control were plotted as an average of duplicates with standard error.

Mechanisms

Many NPs cause production of Reactive Oxygen Species (ROS) in bacteria with which they interact. This ROS damages cellular structures, and this is one of the mechanisms by which nanoparticles are lethal to bacterial cells [28]. To determine whether ROS are produced by bacteria in response to $Mg(OH)_2$ and Cu-infused $Mg(OH)_2$ NPs, the cell permeant dye 5-(and-6)-carboxy-2′,7′-dichlorodihydrofluorescein diacetate (carboxy-H_2DCFDA) was introduced to the cells. Within the cell, carboxy-

H_2DCFDA is converted intracellularly to the intermediate carboxy-DCFH, which in the presence of ROS, can be oxidized to a green fluorescent molecule, namely carboxy-DCF (Molecular Probes, ThermoFisher). The addition of DAPI, a blue fluorescent permeant DNA-binding dye, allows all bacterial cells to be located, and images captured at different wavelengths can then be overlapped to identify cells which produce ROS. In particular, overlap of the blue fluorescent DAPI image and the green fluorescent carboxy-DCF image allows identification of the ROS-producing bacteria.

In (**Figure 16**) the fluorescent signals of ROS positive *E. coli* cells in the presence to $Mg(OH)_2$ NPs suspended in liquid are shown in (**Figure 16 d**). When cells are incubated with PP disks with $Mg(OH)_2$ embossed on the disk surface, fluorescent ROS positive *E. coli* are also seen in (**Figure 16 e**). The average number of fluorescent signals is similar in each case as shown in (**Table 1**, and **Figure 17**).
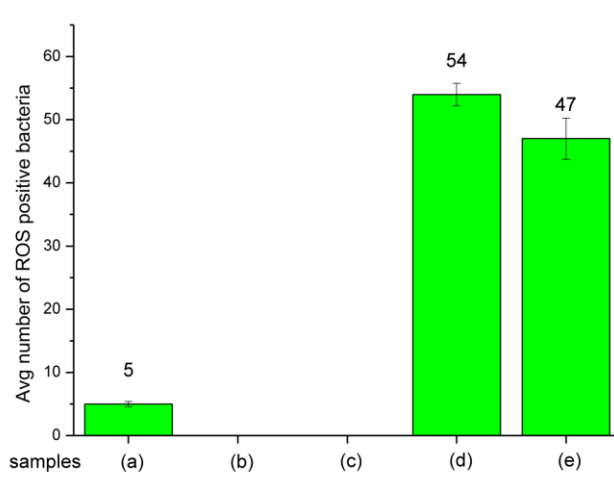
Mg(OH)$_2$ biocide – Mode of Action
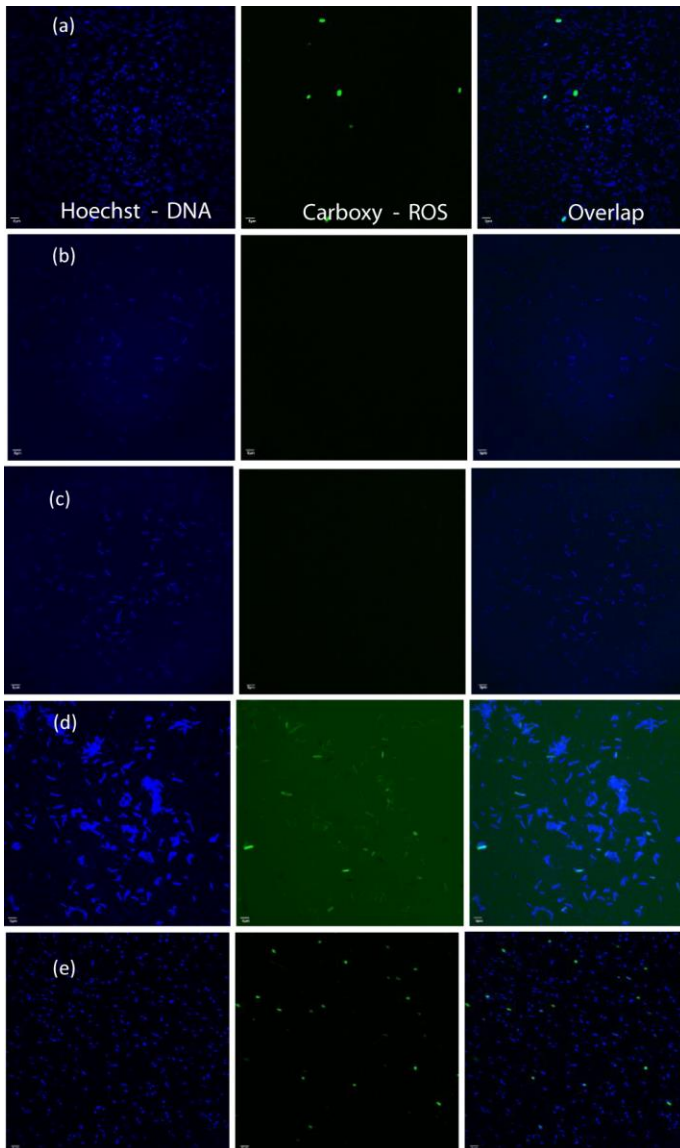
Figure 16: The fluorescent images for samples: (a) bacterial suspension + TBHP, (b) bacterial suspension alone, (c) bacterial suspension + control disk, (d) bacterial suspension + Mg(OH)$_2$ particles, and (e) bacterial suspension + plastic disk coated with Mg(OH)$_2$.

Table 1: Average number of ROS positive bacteria when exposed to Mg(OH)$_2$ biocide.

Sample	Avg number of ROS positive bacteria
(a) Bacterial Suspension + TBHP	5
(b) Bacterial Suspension Alone	0
(c) Bacterial Suspension + Control Disk	0
(d) Bacterial Suspension + Mg(OH)$_2$ particles	54
(e) Bacterial Suspension + Plastic Disk Coated with Mg(OH)$_2$	47

Figure 17: Average number of ROS positive bacteria when exposed to Mg(OH)$_2$ biocide: (a) bacterial suspension + TBHP, (b) bacterial suspension alone, (c) bacterial suspension + control disk, (d) bacterial suspension + Mg(OH)$_2$ particles, (e) bacterial suspension + plastic disk coated with Mg(OH)$_2$.

The results in (**Figure 16** and **Figure 17**) show that Mg(OH)$_2$ NPs induce ROS production in *E. coli*. The ROS production in the bacterial populations exposed to suspensions of Mg(OH)$_2$ NPs (10,000 ppm in PBS) was 14.89 % higher than that produced in *E. coli* populations exposed to Mg(OH)$_2$ NPs that were embossed onto the surfaces of PP disks. The reason could be becuase the suspension provide a better interaction between the **microorganism and the NPs**, and that is why the NPs would produce a higher ROS as seen in (**Figure 17**, and **Table 1**). In the case of PP disks that were embossed with Mg(OH)$_2$ NPs, there would be less interaction between the microorganism and the NPs because the NPs were incorporated to the surface and thus are confined to that surface compared to Nanoparticles in suspension that will interact with bacteria with greater frequency. Magnesium

hydroxide is insoluble (K_{sp}= 5.61 × 10^{-12}) and consequently no ionization will occur in these assays, and thus ROS production occurs as a result of the direct interaction between bacteria and the nanoplatelets.

Cu-infused Mg(OH)$_2$ biocide – Mode of Action

In (**Figure 18** and **Figure 19**) fluorescent, ROS positive *E. coli* cells that had emerged in response to exposure to a suspension of Cu-infused Mg(OH)$_2$ NPs (**Figure 18 d**) and to PP disks with Mg(OH)$_2$ affixed to the disk surfaces (**Figure 18 e**) are shown. The ROS production in the bacterial populations exposed to suspensions of Cu-infused Mg(OH)$_2$ NPs was 196.67 % higher than that produced in *E. coli* populations exposed to Cu-infused Mg(OH)$_2$ NPs that were embossed onto the surfaces of PP disks. The reason could be becuase the suspension provide a better interaction between the microorganism and the NPs, and that is why the NPs would produce a higher ROS as seen in (**Figure 19**, and **Table 2**). In the case of PP disks that were embossed with Cu-infused Mg(OH)$_2$ NPs, there would be less interaion between the microorganism and the NPs because the NPs were attached to the disks surface from one side and exposed to the microorganism from the other side.

However, these results are broadly similar to those observed for the Mg(OH)$_2$ NPs.
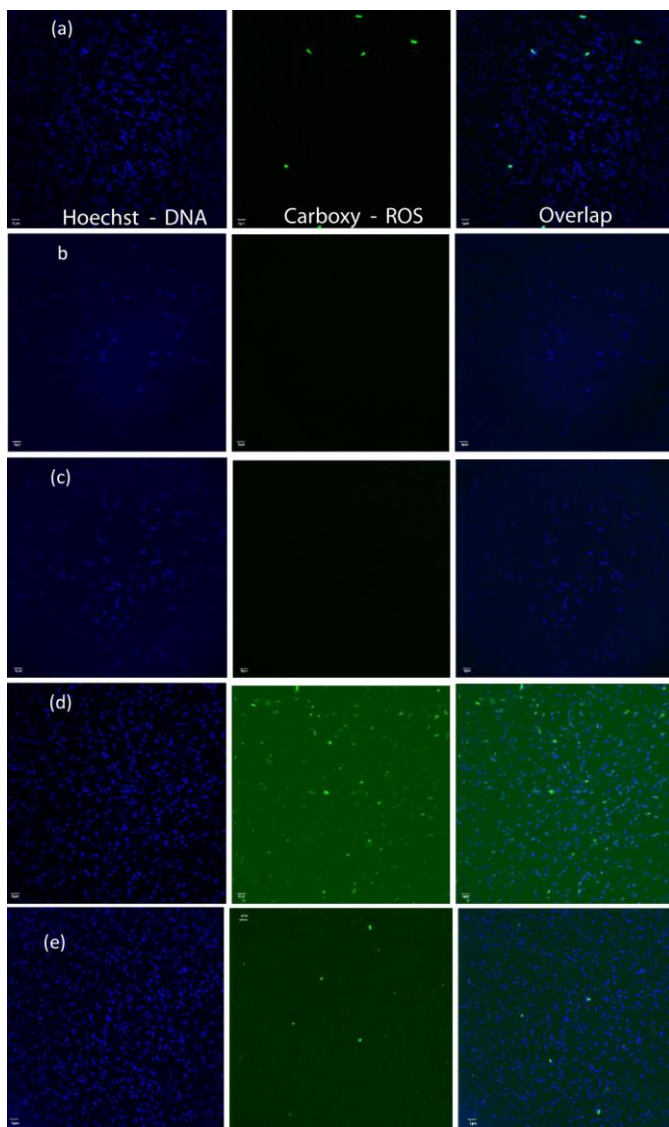
Figure 18: The fluorescent images of samples: (a) bacterial suspension + TBHP, (b) bacterial suspension alone, (c) bacterial suspension + control disk, (d) bacterial suspension + Cu-infused Mg(OH)$_2$ particles, and (e) bacterial suspension + plastic disk coated with Cu-infused Mg(OH)$_2$.

Table 2: Average number of ROS positive bacteria when exposed to Cu-infused Mg(OH)$_2$ biocide.

Sample	Avg number of ROS positive bacteria
(a) Bacterial Suspension + TBHP	5
(b) Bacterial Suspension Alone	0
(c) Bacterial Suspension + Control Disk	0
(d) Bacterial Suspension + Cu-infused Mg(OH)$_2$ particles	89
(e) Bacterial Suspension + Plastic Disk Coated with Cu-infused Mg(OH)$_2$	30
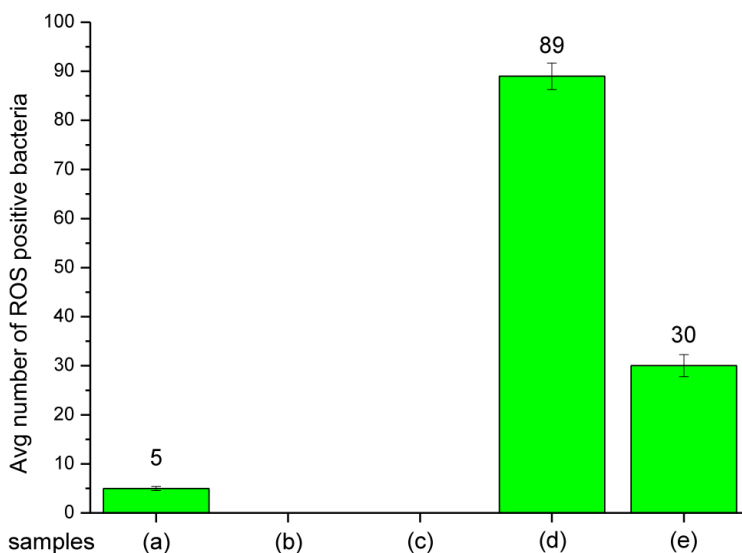
Figure 19: Average number of ROS positive bacteria detected following exposure to the Cu-infused Mg(OH)$_2$ biocides: (a) bacterial suspension + TBHP, (b) bacterial suspension alone, (c) bacterial suspension + control disk, (d) bacterial suspension + Cu-infused Mg(OH)$_2$ particles, and (e) bacterial suspension + plastic disk coated with Cu-infused Mg(OH)$_2$.

ROS production in the *E. coli* populations that had been exposed to Cu-infused Mg(OH)$_2$ NPs in suspension is approxamitly two times higher than that produced in *E. coli* populations that were exposed to Cu-infused Mg(OH)$_2$ NPs which had been embossed onto the surfaces of PP disks (**Figure 19**, and **Table 2**). This is in contrast to the results observed for Mg(OH)$_2$ (**Figure 17**). Mg(OH)$_2$ is essentially insoluble while Cu-infused Mg(OH)$_2$ includes the highly soluble Cu^{2+} ion. The difference in ROS production due to exposure to the suspension versus the surface bound Cu-infused Mg(OH)$_2$ may be due to the ionizaton and

release of anti-microbial Cu^{2+} ions in the suspension while these ions remain assosiated with PP disks when Cu-infused $Mg(OH)_2$ NPs are embossed on the surface. Metal ions, including copper ions, can generate ROS in bacteria. The results in (**Figure 19**) imply that ionization may contribute to ROS production when Cu-infused $Mg(OH)_2$ NPs are present in suspension.

Production of intracellular ROS is a principal mechanism of NP toxicity [28]. The NP-elicited production of ROS within bacterial cells may explain the bacteriocidal effect of the coated discs. Altenative mechanisms must be used to explain the destruction of the non-cellular, enveloped Coronavirus.

Discussion

The SEM images and EDX spectra of $Mg(OH)_2$ and Cu-infused $Mg(OH)_2$ crystals shown in (**Figure 7** and **Figure 8**), respectivly, confirmed that the $Mg(OH)_2$ particles had a platelet-shaped morphology. Meanwhile, they also revealed that the Cu-infused $Mg(OH)_2$ crystals had two different shapes; nanoplatelets for $Mg(OH)_2$, and spherical for Cu. Both crystals are attached together from the outer surface due to the ion exchange phenomena. The platelet-shaped $Mg(OH)_2$ particles had a width in the range of 160-260 nm and a thickness of 30-50 nm thickness, while the spherical Cu particles had a diameter in the range of 100-280 nm. The SEM images and EDX spectra of the surfaces of compounded and injection molded PP disks bearing 5 wt.% $Mg(OH)_2$ and 5 wt.% Cu-infused $Mg(OH)_2$ shown in (**Figure 9** and **Figure 10**), respectively, do not show any evidence of biocidal crystals on the outer surfaces of the PP disks. In agreement with this observation, when the interior of the componded disks are viewed by SEM and EDX, as shown in (**Figure 20** and **Figure 21**), biocrystals are seen to be entirely within the structure and appear to be agglomerated. The SEM images of the surface embossed PP disks shown in (**Figure 11** (**B**) and **Figure 11** (**C**), respectively) show a complete coverage with the biocidal crystals. The PP surface that had been thermally embossed with $Mg(OH)_2$ NPs is smooth and evenly packed. In contrast, the PP surface bearing the Cu-infused $Mg(OH)_2$ NPs, which are composed of both platelet and spherically shaped

crystals, is less evenly packed so that it exhibits a slightly rougher surface due to the mixture of crystal morphologies.
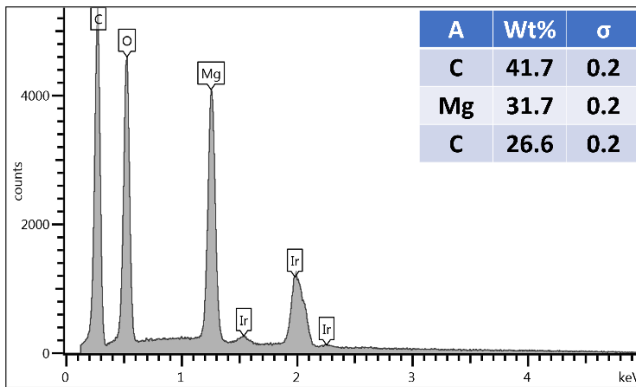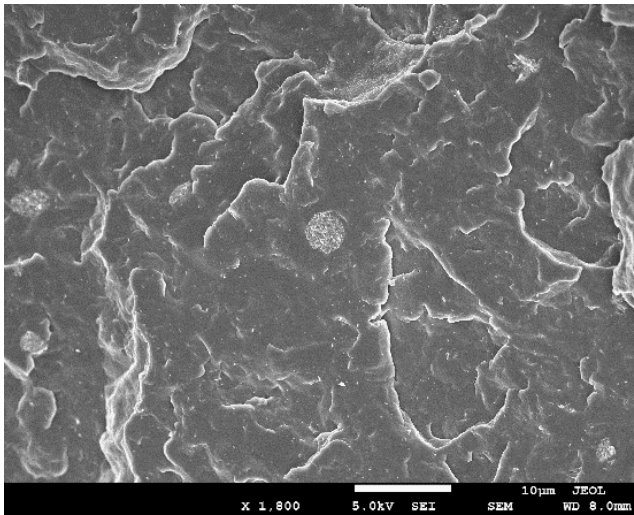
Figure 20: Cross-sectional view of PP that had been compounded with 5 wt.% $Mg(OH)_2$.

A	Wt%	σ
O	37.6	0.2
Mg	21.2	0.2
C	15.8	0.2
Cu	15.5	0.2
Cl	8.9	0.3
S	0.9	0.2
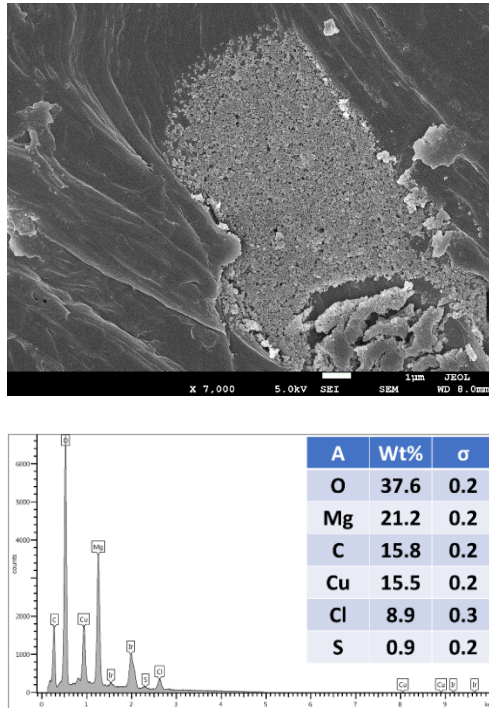
Figure 21: Cross-sectional view of PP compounded with 5 wt.% Cu-infused $Mg(OH)_2$.

The melt-compounded and injection molded PP with 5 wt.% $Mg(OH)_2$ had a T_m of 166.13 ± 0.81 °C, and that with 5 wt.% Cu-infused $Mg(OH)_2$ had a T_m of 165.45 ± 0.11 °C, while the PP control had a T_m of 165.43 ± 0.78 °C. The PP that had been thermally embossed with $Mg(OH)_2$ NPs showed a T_m of 164.88 ± 0.01 °C, and that which had been thermally embossed with Cu-infused $Mg(OH)_2$ NPs showed a T_m of 166.05 ± 0.32 °C compared to the PP control which had a T_m of 165.43 ± 0.78 °C, as shown in (**Figure 22**). The melt-compounded and injection molded PP with 5 wt.% $Mg(OH)_2$ showed a T_c of 119.64 ± 0.73 °C, and that with 5 wt.% Cu-infused $Mg(OH)_2$ had a T_c of 116.98 ± 0.33 °C. The PP that had been thermally embossed with $Mg(OH)_2$ NPs showed a T_c of 118.87 ± 0.13 °C, while that which had been thermally embossed with Cu-infused $Mg(OH)_2$ NPs had a T_c of 119.14 ± 0.36 °C compared to the PP control which had a T_c of 117.31 ± 0.30 °C, as shown in (**Figure 23**). The melt-compounded and

injection molded PP with 5 wt.% $Mg(OH)_2$ had 8.34 % higher crystallinity (%) (43.63 ± 0.83 %), and that with 5 wt.% Cu-infused $Mg(OH)_2$ had 2.54 % lower crystallinity (%) (39.00 ± 0.83 %) compared to the PP control (39.99 ± 0.61 %). The PP that had been thermally embossed with $Mg(OH)_2$ NPs had 10.56 % higher crystallinity (%) (44.71 ± 5.53 %), and that which had been thermally embossed with Cu-infused $Mg(OH)_2$ NPs had 2.54 % lower crystallinity (%) (39.00 ± 2.64 %) compared to the PP control (T_c = 39.99 °C ± 0.61), as shown in (**Table 3**). Overall, both biocidal additives had slightly influenced the crystallinity (%) of the PP samples.

Table 3: Crystallinity of PP samples obtained from DSC measurements.

| Samples	ΔH_m (J/g)	T_m (°C)	T_c (°C)	Crystallinity (%)
Neat PP	83.59 ± 1.27	165.43 ± 0.78	117.31 ± 0.30	39.99 ± 0.61
PP 5 wt.% $Mg(OH)_2$ (compounded)	86.62 ± 1.64	166.13 ± 0.81	119.64 ± 0.73	43.63 ± 0.83
PP $Mg(OH)_2$ (thermally embossed)	92.52 ± 11.43	164.88 ± 0.01	118.87 ± 0.13	44.71 ± 5.53
PP 5 wt.% Cu-infused $Mg(OH)_2$ (compounded)	88.56 ± 2.00	165.45 ± 0.11	116.98 ± 0.33	44.60 ± 1.01
PP Cu-infused $Mg(OH)_2$ (thermally embossed)	80.69 ± 5.47	166.05 ± 0.32	119.14 ± 0.36	39.00 ± 2.64

The TGA characterization data shown in (**Table 4**) indicate that $Mg(OH)_2$ powder has lost 5 wt.% of its original weight at 206.52 ± 0.06 °C, and the Cu-infused $Mg(OH)_2$ powder has lost 5 wt.% of its original weight at 290.39 ± 0.78 °C.

Table 4: The temperature at which various PP samples underwent 5% weight loss as determined via TGA measurements.

| Sample	The temperature at which 5% weight loss occurred (°C)
$Mg(OH)_2$ Powder	206.52 ± 0.06
Cu-infused $Mg(OH)_2$ Powder	290.39 ± 0.78
Neat PP	337.54 ± 0.03
PP 5 wt.% $Mg(OH)_2$ (compounding)	340.46 ± 0.07
PP 5 wt.% $Mg(OH)_2$ (thermal embossing)	336.26 ± 0.06
PP 5 wt.% Cu-infused $Mg(OH)_2$ (compounding)	350.10 ± 1.39
PP 5 wt.% Cu-infused $Mg(OH)_2$ (thermal embossing)	322.44 ± 0.01

The most significant weight reduction (5 to 40 %) has occurred around 330 and 450 °C (**Figure 24**) due to the high-temperature oxidization (HTO) of metal and metal hydroxide [38]. $Mg(OH)_2$ is a metal hydroxide and Cu-infused $Mg(OH)_2$ is a combination of both metal (Cu) and magnesium hydroxide ($Mg(OH)_2$). The HTO would cause these particles to start releasing the H_2O around 330 °C, and it will reach a complete drying around 450 °C. According to the TGA data shown in (**Figure 24**), if $Mg(OH)_2$ and Cu-infused $Mg(OH)_2$ NPs are heated up to 450 °C, they will be

converted into MgO and Cu-infused MgO which are expected to have even a stronger anti-microbial activity compared to the metal hydroxide. The PP that had been compounded with 5 wt.% $Mg(OH)_2$ and Cu-infused $Mg(OH)_2$ have lost 5 % of their weights at (340.46 ± 0.07 and 350.10 ± 1.39 °C, respectively) which were comparatively higher temperatures (by 0.6 and 3.4 %, respectively) than that observed for neat PP (337.54 ± 0.03 °C). The PP samples that had been thermally embossed with 10 mg/mL $Mg(OH)_2$ and Cu-infused $Mg(OH)_2$ have lost 5 % of their weights at (336.26 ± 0.06, and 332.44 ± 0.01 °C, respectively) which was comparatively lower (by 0.6 and 1.8 %, respectively) than neat PP (337.54 ± 0.03 °C). The loss of 5 % in weight was higher in the PP compounded material compared to that observed for the neat PP because the particles were embedded within the PP matrix, and the particles in the PP composite would need a longer time to release the H_2O. Meanwhile, the loss of 5 % in weight was observed at lower temperatures in PP thermally embossed samples compared to the neat PP because the particles were thermally embossed on the PP surface, and the particles would react faster to the HTO and release the H_2O contents. Overall, neither of the biocidal additives influence the thermal stability of the PP samples.
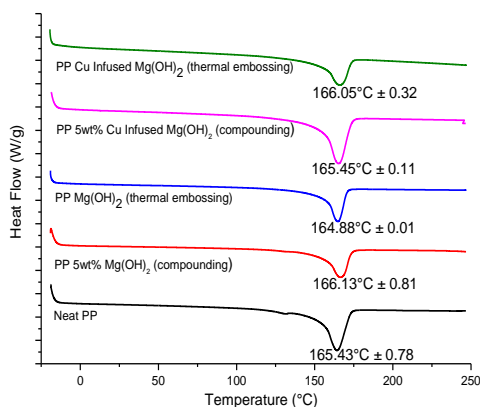
Figure 22: The Tm values obtained from the DSC data for various samples.
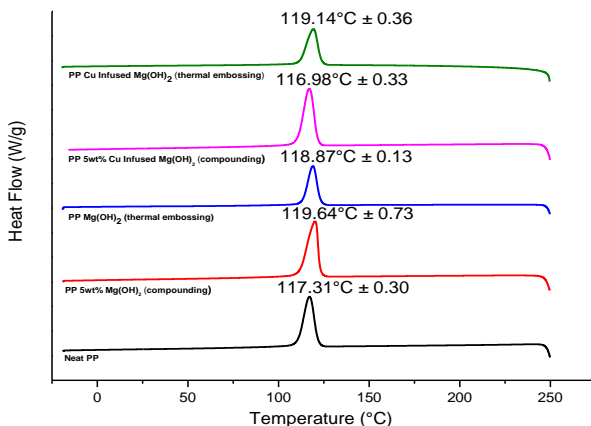
Figure 23: The Tc values obtained from the DSC data for various samples.
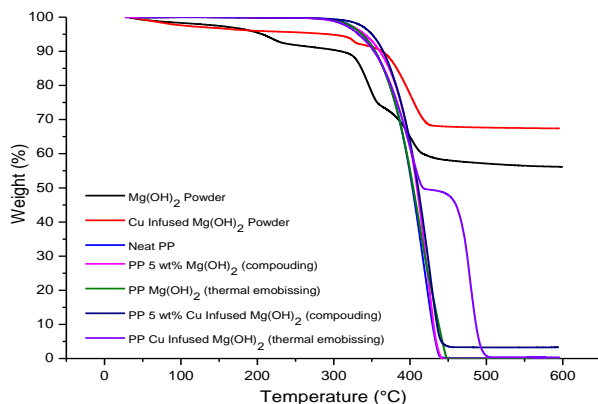
Figure 24: TGA characterization data obtained for (a) powder samples of anti-microbial agents, (b) neat PP, (c) melt compounding PP, (d) and thermally embossed PP.

E. coli is a common test bacteria and is among the five bacterial species that are most responsible for illness and death worldwide [39]. The anti-microbial testing data shown in (**Figure 12**) indicates that the PP disks prepared by melt-compounding and injection molding bearing 5 wt.% $Mg(OH)_2$ and 5 wt.% Cu-infused $Mg(OH)_2$ (where the crystals are within the matrix of the

polymer) do not exhibit anti-microbial activity. There is no migration of anti-microbial material to and beyond the surface of the polymer, and apparently no migration of Cu ions from the polymer to a degree where bacteria are inhibited (**Figure 12 C** and **Figure 16 D**). When $Mg(OH)_2$ NPs or Cu-infused $Mg(OH)_2$ NPs are "thermally embossed" to the surface of the PP polymer disks, bacteria that come into contact with these surfaces are killed (**Figure 13 C** and **Figure 13 D**). In these assays, the PP disks that had been embossed with $Mg(OH)_2$ and Cu-infused $Mg(OH)_2$ NPs showed (2.6 ± 0.08 and 0.63 ± 0.04 log reduction within 4 h, respectively) which was equivalent to (98.90 and 2.28 % reduction, respectively) from the negative control sample (0.64 ± 0.14). A significant difference in the initial rate of killing was observed with the anti-microbial effect of PP disks that had been embossed with the $Mg(OH)_2$ NPs, acting drastically faster than the PP disks that had been embossed with the Cu-infused $Mg(OH)_2$ NPs after 4 h. However, both coatings achieved complete elimination of bacteria when they had been assayed at 24 h. The PP disks that were embossed with $Mg(OH)_2$ and Cu-infused $Mg(OH)_2$ NPs showed (6.48 ± 0.08 and 6.81 ± 0.55 log reduction within 24 h, respectively) which were both equivalent to (99.99996 % reduction) from the negative control sample (0.58 ± 0.03).

An anti-viral study was conducted to evaluate the abilities of the $Mg(OH)_2$ NPs suspension and Cu-infused $Mg(OH)_2$ NPs suspension to inactivate SARS-CoV-2 virus infectivity. In solution after 4 h of incubation at room temperature, the $Mg(OH)_2$ NPs suspension, at 0.25 % reduced SARSCoV-2 virus titers in the solution by 2.5×10^3 PFU/mL or 29.4 %, while the Cu-infused $Mg(OH)_2$ NPs suspension, at 0.25 % reduced titers by 8.1×10^3 PFU/mL or 95.3 % as shown in (**Figure 15**). These assays involved a physico-chemical assault on the virus structure followed by an assay of the ability of the assaulted virus to successfully infect mammalian cells. While damage to bacterial cell walls may cause leakage of cell material from a pressurized cell and loss of viability, a virus enveloped by a cell membrane may maintain infectivity until severe disruption occurs such that the nucleic acid is degraded, or key surface proteins are inactivated. Alteration of concentrations may produce more rapid

virus destruction. The aim of experimentally testing the anti-viral activity in aqueous solutions was to simply confirm the anti-viral properties for the pure $Mg(OH)_2$ and Cu-infused $Mg(OH)_2$ NPs. The thermally embossed PP material with the anti-microbial NPs should provide the desired anti-viral activity because the NPs would be affixed on the surface, and it would be able to eliminate the viruses in the same mechanism observed with the *E.coli* in (**Figure 13**). $Mg(OH)_2$ NPs also exhibited an increased anti-bacterial activity not only against Gram-negative bacteria such as *Escherichia coli* (*E. coli*) but also against Gram-positive bacteria such as *Staphylococcus aureus* (*S. auresus*) and *Staphylococcus epidermis* (*S. Epidermis*) [40].

A previous study has indicated that anti-bacterial drugs derived from $Mg(OH)_2$ NPs have the potential to be effective [13,19,41-43]. However, the mechanism of action through which $Mg(OH)_2$ NPs exhibit their bactericidal activity has yet to be well studied [13,14,44]. When they used $Mg(OH)_2$ NPs manufactured by Aqua Resources Corp (similar to those used in this study), Dong et al. showed that physical contact was necessary to kill *E. coli* cells, but that bacterial destruction did not appear to involve the uptake of nanoplatelets by cells [41]. Dong et al. hypothesized that the direct presence of surface areas with a high concentration of hydroxyl group (–OH) groups of $Mg(OH)_2$ NPs would be damaging to the bacterial cell walls [41,44]. Pan et al. conducted microbial experiments with $Mg(OH)_2$ NPs that were manufactured by three different methods and showed that perturbation of the bacterial membranes occurred when *E. coli* cells were exposed to $Mg(OH)_2$ NPs, but studies using energy-dispersive X-ray spectroscopy (EDX) found no evidence for internalization of $Mg(OH)_2$ NPs nor were there elevated Mg levels within cells [13]. Dong et al. showed that neither high pH nor high concentrations of magnesium ions ($MgSO_4$) showed lethality [41]. Nakamura et al. created mutant bacterial strains where genes for various magnesium transport systems had been deleted, and used them to demonstrate that magnesium uptake had no effect on the killing potency of $Mg(OH)_2$ NPs. Physical damage was assigned as a principal cause of bacterial cell death [45]. Pan et al. proposed that the $Mg(OH)_2$ NPs attach to the surface of the bacterial cells

due to charge attraction before rupturing the cell walls and killing the bacteria [13].

Physical damage to bacterial cell walls with concomitant leakage of cell contents, loss of integrity of membrane bound enzymatic systems, and dissipation of electron motive force are all potent assaults upon bacterial viability. The current work demonstrated that $Mg(OH)_2$ NPs (like many other nanoparticles) cause the production of ROS in bacteria with which they interact [46]. This is the first demonstration of ROS production being induced by $Mg(OH)_2$ and Cu-infused $Mg(OH)_2$ nanoplatelets. PP embossed with $Mg(OH)_2$ NPs produced about 1.5 x the amount of ROS in bacterial cells as was produced by Cu-infused $Mg(OH)_2$ NPs. The initial killing rate of $Mg(OH)_2$ NPs is faster (at 4 hours) however by 24 hours both embossed discs had completely eliminated E.coli from the pod chamber. This end point may have been achieved earlier by the $Mg(OH)_2$ NPs and more detailed time courses are being conducted. This is consistent with their similar potency in destroying *E. coli* in thermally embossed PP surfaces, referring to (**Figure 13**). The results in (**Figure 16** and **Figure 17**) show similar ROS production in *E. coli* exposed to $Mg(OH)_2$ NPs suspension and to $Mg(OH)_2$ NPs adhered to PP surfaces. $Mg(OH)_2$ NPs are insoluble and ionization will not contribute to ROS production. In contrast, a suspension of Cu-infused $Mg(OH)_2$ NPs produced two times more ROS than PP-bound Cu-infused $Mg(OH)_2$ NPs (**Figure 19**). Cu ions are highly soluble and can produce ROS in bacteria [1,2]. The reduced ROS level for PP-bound Cu-infused $Mg(OH)_2$ NPs (**Figure 19**) implies that Cu ionization and migration into the media does not occur as readily as when the NPs are embossed onto the PP surface. This may have positive implications in terms of rendering surfaces anti-bacterial properties without the problem associated with the leaching of agents from a treated surface. The contribution of membrane disruption and ROS production to the killing of bacteria may be varied for different types of nanoparticles and the role of each mechanism in killing Gram-positive and Gram-negative pathogens remains to be determined.

Several research groups have reported non-ROS mediated anti-microbial activity of MgO nanoparticles. Leung et al. demonstrated destruction of bacteria by MgO nanoparticles in the

absence of ROS [47]. Surface modification of MgO NPs that reduce of ROS production by the nanoparticle resulted in increased non-ROS mediated cell toxicity, with acid/base reaction at the MgO/bacteria surface being proposed as a significant mechanism [48]. Modulating surface modification to reveal more oxygen vacancies can increase ROS production and a synergistic effect of ROS- and non-ROS-mechanisms was proposed as the mechanisms by which MgO nanoparticles normally work [49]. The revelation of non-ROS mediated cell destruction decouples anti-microbial potential from ROS production. Both mechanisms are in play and surface modifications, such as the inclusion of Copper atoms on the nanoplatelet surface, as has been demonstrated in the work cited above, will alter the relative impact of ROS- and non-ROS mechanisms of action.

As such, we believe that direct contact between $Mg(OH)_2$ nanoplatelets and Cov-2 virus, in suspension may cause lipid and protein perturbations on this enveloped virus causing collapse of the viral structure, though the relative effects of ROS cannot at this point be determine

Conclusion

Our findings suggest that $Mg(OH)_2$ and Cu-infused $Mg(OH)_2$ NPs have strong anti-bacterial and anti-viral activities. ROS is produced by both forms of nanoplatelets and is likely to be a significant mode of anti-bacterial action. Additional, non-ROS mechanisms involving direct contact between NPs and the bacterial surface my also play a role. It is interesting that surfaces embossed with $Mg(OH)_2$ and Cu-infused $Mg(OH)_2$ NPs and pure anti-bacterial NPs suspensions eliminate bacteria with similar efficacy. This may relate to speed of action or the relative importance of ROS-mediated and non-ROS mediated killing. Thermal surface embossing showed a 6.5 log reduction of *E. coli* in 24 h. Similarly, $Mg(OH)_2$ and Cu-infused $Mg(OH)_2$ NPs exhibit anti-viral activity against (SARS-CoV-2) covid-19 virus. This efficacy is supported by SEM-EDX data where the pure NPs and surfaces embossed with those NPs have similar chemical compositions. Thus, surface embossing techniques hold the promise for broad applications in both commercial and household settings.

References

1. 7.7 million people die from bacterial infections every year – 2022 – ReAct. ReAct 2022.
2. Global burden of bacterial antimicrobial resistance in 2019: a systematic analysis. Lancet (London, England). 2022; 399: 629-655.
3. Rahman MT, Sobur MA, Islam MS, Ievy S, Hossain MJ, et al. Zoonotic Diseases: Etiology, Impact, and Control. Microorganisms. 2020; 8.
4. Ghosh TS, Shanahan F, O'Toole PW. The gut microbiome as a modulator of healthy ageing. Nature Reviews Gastroenterology & Hepatology. 2022; 19: 565-584.
5. Rodríguez-Lázaro D, Cook N, Ruggeri FM, Sellwood J, Nasser A, et al. Virus hazards from food, water and other contaminated environments. FEMS Microbiology Reviews. 2012; 36: 786-814.
6. Fauvel B, Cauchie HM, Gantzer C, Ogorzaly L. Influence of physico-chemical characteristics of sediment on the in situ spatial distribution of F-specific RNA phages in the riverbed. FEMS microbiology ecology. 2019; 95.
7. Cassidy SS, Sanders DJ, Wade J, Parkin IP, Carmalt CJ, et al. Antimicrobial surfaces: A need for stewardship? PLoS pathogens. 2020; 16: e1008880.
8. Choudhury M, Bindra HS, Singh K, Singh AK, Nayak R. Antimicrobial polymeric composites in consumer goods and healthcare sector: A healthier way to prevent infection. 2022; 33: 1997-2024.
9. Uddin TM, Chakraborty AJ, Khusro A, Zidan BRM, Mitra S, et al. Antibiotic resistance in microbes: History, mechanisms, therapeutic strategies and future prospects. Journal of infection and public health. 2021; 14: 1750-1766.
10. Zhu Y, Tang Y, Ruan Z, Dai Y, Li Z, et al. Mg(OH)2 nanoparticles enhance the antibacterial activities of macrophages by activating the reactive oxygen species. Journal of Biomedical Materials Research Part A. 2021; 109.
11. Raza S, Matuła K, Karoń S, Paczesny J. Resistance and Adaptation of Bacteria to Non-Antibiotic Antibacterial Agents: Physical Stressors, Nanoparticles, and Bacteriophages. Antibiotics (Basel, Switzerland). 2021; 10.

12. Zheng S, Bawazir M, Dhall A, Kim HE, He L, et al. Implication of Surface Properties, Bacterial Motility, and Hydrodynamic Conditions on Bacterial Surface Sensing and Their Initial Adhesion. Frontiers in bioengineering and biotechnology. 2021; 9: 643722.

13. Pan X, Wang Y, Chen Z, Pan D, Cheng Y, et al. Investigation of antibacterial activity and related mechanism of a series of nano-$Mg(OH)_2$. ACS Appl Mater Interfaces. 2013; 5: 1137-1142.

14. Ferdous Z, Nemmar A. Health Impact of Silver Nanoparticles: A Review of the Biodistribution and Toxicity Following Various Routes of Exposure. International journal of molecular sciences. 2020; 21.

15. Cheeseman S, Christofferson AJ, Kariuki R, Cozzolino D, Daeneke T, et al. Antimicrobial Metal Nanomaterials: From Passive to Stimuli-Activated Applications. 2020; 7: 1902913.

16. Alkarri S, Sharma D, Bergholz TM, Rabnawaz M. Fabrication methodologies for antimicrobial polypropylene surfaces with leachable and nonleachable antimicrobial agents. Journal of Applied Polymer Science. 2023; e54757.

17. Geddes L. Antimicrobial Surface.

18. Brandelli A, Ritter AC, Veras FF. Antimicrobial Activities of Metal Nanoparticles. In: Rai PDM, Shegokar PDR, editors. Metal Nanoparticles in Pharma. Berlin: Springer International Publishing. 2017; 337-363.

19. Dong C, Song D, Cairney J, Maddan OL, He G, et al. Antibacterial study of Mg(OH)2 nanoplatelets. Materials Research Bulletin. 2011; 46: 576-582.

20. Brandelli A, Ritter A, Veras F. Antimicrobial Activities of Metal Nanoparticles. 2017; 337-363.

21. Singha P, Locklin J, Handa H. A Review of the Recent Advances in Antimicrobial Coatings for Urinary Catheters. Acta Biomaterialia. 2016; 50.

22. Alves PM, Barrias CC, Gomes P, Martins MCL. Smart biomaterial-based systems for intrinsic stimuli-responsive chronic wound management. Materials Today Chemistry. 2021; 22: 100623.

23. Sánchez-López E, Gomes D, Esteruelas G, Bonilla L, Lopez-Machado AL, et al. Metal-Based Nanoparticles as Antimicrobial Agents: An Overview. 2020; 10: 292.

24. Hu X, Zhang H, Wang Y, Shiu BC, Lin JH, et al. Synergistic antibacterial strategy based on photodynamic therapy: Progress and perspectives. Chemical Engineering Journal. 2022; 450: 138129.
25. Imani MM, Safaei M. Optimized Synthesis of Magnesium Oxide Nanoparticles as Bactericidal Agents. Journal of Nanotechnology. 2019; 2019: 6063832.
26. Seifi T, Kamali AR. Anti-pathogenic activity of graphene nanomaterials: A review. Colloids and surfaces. B, Biointerfaces. 2021; 199: 111509.
27. Wang L, Hu C, Shao L. The antimicrobial activity of nanoparticles: present situation and prospects for the future. International journal of nanomedicine. 2017; 12: 1227-1249.
28. Luan G, Hong Y, Drlica K, Zhao X. Suppression of Reactive Oxygen Species Accumulation Accounts for Paradoxical Bacterial Survival at High Quinolone Concentration. Antimicrobial agents and chemotherapy. 2018; 62.
29. Motoike K, Hirano S, Yamana H, Onda T, Maeda T, et al. Antiviral activities of heated dolomite powder. Biocontrol science. 2008; 13: 131-138.
30. Zhu Y, Tang Y, Ruan Z, Dai Y, Li Z, et al. Mg(OH)2 nanoparticles enhance the antibacterial activities of macrophages by activating the reactive oxygen species. Journal of Biomedical Materials Research Part A. 2021; 109: 2369-2380.
31. Esteban Florez F, Khajotia S. 4 Interactions between Oral Bacteria and Antibacterial Polymer-Based Restorative Materials. 2020.
32. Zhong Y, Xiao H, Seidi F, Jin Y. Natural Polymer-Based Antimicrobial Hydrogels without Synthetic Antibiotics as Wound Dressings. Biomacromolecules. 2020; 21: 2983-3006.
33. Brandrup J, Immergut EH, Grulke EA, Abe A, Bloch DR. Polymer handbook. New York: Wiley. 1999.
34. Maddan OL. Nanoplatelet copper hydroxides and methods of preparing same. Google Patents. 2008.
35. Maddan OL. Hydroxides monolayer nanoplatelet and methods of preparing same. Google Patents. 2022.
36. BEI resources web portal > home. BEI resources 2023.

37. Perez N. High-Temperature Oxidation. In: Perez N, editor. Electrochemistry and Corrosion Science. Berlin: Springer International Publishing. 2016; 389-425.

38. Global mortality associated with 33 bacterial pathogens in 2019: a systematic analysis for the Global Burden of Disease Study 2019. Lancet (London, England). 2022; 400: 2221-2248.

39. Alves MM, Batista C, Mil-Homens D, Grenho L, Fernandes MH, et al. Enhanced antibacterial activity of Rosehip extract-functionalized Mg(OH)(2) nanoparticles: An in vitro and in vivo study. Colloids and surfaces. B, Biointerfaces. 2022; 217: 112643.

40. Dong C, Cairney J, Sun Q, Maddan OL, He G, et al. Investigation of Mg(OH)2 nanoparticles as an antibacterial agent. Journal of Nanoparticle Research. 2010; 12: 2101-2109.

41. Lih E, Kum CH, Park W, Chun SY, Cho Y, et al. Modified magnesium hydroxide nanoparticles inhibit the inflammatory response to biodegradable poly (lactide-co-glycolide) implants. 2018; 12: 6917-6925.

42. Meng Y, Zhang D, Jia X, Xiao K, Lin X, et al. Antimicrobial activity of nano-magnesium hydroxide against oral bacteria and application in root canal sealer. 2020; 26: e922920-922921.

43. Dong C, He G, Zheng W, Bian T, Li M, et al. Study on antibacterial mechanism of Mg (OH) 2 nanoparticles. 2014; 134: 286-289.

44. Nakamura Y, Okita K, Kudo D, Phuong DND, Iwamoto Y, et al. Magnesium Hydroxide Nanoparticles Kill Exponentially Growing and Persister Escherichia coli Cells by Causing Physical Damage. 2021; 11: 1584.

45. Yu Z, Li Q, Wang J, Yu Y, Wang Y, et al. Reactive Oxygen Species-Related Nanoparticle Toxicity in the Biomedical Field. Nanoscale Res Lett. 2020; 15: 115.

46. Leung YH, Ng AM, Xu X, Shen Z, Gethings LA, et al. Mechanisms of antibacterial activity of MgO: non-ROS mediated toxicity of MgO nanoparticles towards Escherichia coli. Small (Weinheim an der Bergstrasse, Germany). 2014; 10: 1171-1183.

47. Aničić N, Vukomanović M, Koklič T, Suvorov D. Fewer Defects in the Surface Slows the Hydrolysis Rate, Decreases the ROS Generation Potential, and Improves the Non-ROS Antimicrobial Activity of MgO. Small (Weinheim an der Bergstrasse, Germany). 2018; 14: e1800205.
48. Li X, Hong X, Yang Y, Zhao J, Diko CS, et al. Enhanced antibacterial activity of acid treated MgO nanoparticles on Escherichia coli. RSC advances. 2021; 11: 38202-38207.